

Tin Oxide with Controlled Morphology and Crystallinity by Atomic Layer Deposition onto Graphene Nanosheets for Enhanced Lithium Storage

Xifei Li, Xiangbo Meng, Jian Liu, Dongsheng Geng, Yong Zhang, Mohammad Norouzi Banis, Yongliang Li, Jinli Yang, Ruying Li, Xueliang Sun,* Mei Cai, and Mark W. Verbrugge

As one of the most promising negative electrode materials in lithium-ion batteries (LIBs), SnO₂ experiences intense investigation due to its high specific capacity and energy density, relative to conventional graphite anodes. In this study, for the first time, atomic layer deposition (ALD) is used to deposit SnO₂, containing both amorphous and crystalline phases, onto graphene nanosheets (GNS) as anodes for LIBs. The resultant SnO₂-graphene nanocomposites exhibit a sandwich structure, and, when cycled against a lithium counter electrode, demonstrate a promising electrochemical performance. It is demonstrated that the introduction of GNS into the nanocomposites is beneficial for the anodes by increasing their electrical conductivity and releasing strain energy: thus, the nanocomposite electrode materials maintain a high electrical conductivity and flexibility. It is found that the amorphous SnO₂-GNS is more effective than the crystalline SnO₂-GNS in overcoming electrochemical and mechanical degradation; this observation is consistent with the intrinsically isotropic nature of the amorphous SnO₂, which can mitigate the large volume changes associated with charge/discharge processes. It is observed that after 150 charge/discharge cycles, 793 mA h g⁻¹ is achieved. Moreover, a higher coulombic efficiency is obtained for the amorphous SnO₂-GNS composite anode. This study provides an approach to fabricate novel anode materials and clarifies the influence of SnO₂ phases on the electrochemical performance of LIBs.

1. Introduction

The technology of lithium-ion batteries (LIBs) is widely regarded as one of the most promising solutions for the

Dr. X. Li, Dr. X. Meng, J. Liu, Dr. D. Geng, Dr. Y. Zhang, M. N. Banis, Y. Li, J. Yang, R. Li, Prof. X. Sun
Nanomaterials and Energy Lab
Department of Mechanical and Materials Engineering
University of Western Ontario
London, Ontario, N6A 5B9, Canada
E-mail: xsun@eng.uwo.ca

Dr. M. Cai, Dr. M. W. Verbrugge
General Motors R&D Center
Warren, MI 48090-9055, USA

DOI: 10.1002/adfm.201101068



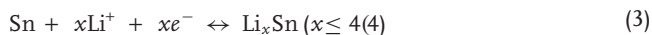
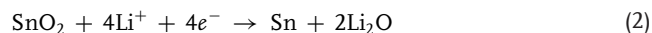
ever-fading fossil-fuel energies in modern society, being capable of providing energy for portable electronics and electric vehicles since the concept of a “rocking-chair” type of rechargeable battery emerged in 1990.^[1–3] In particular, the recent, increased interest in hybrid electric vehicles (HEVs) and plug-in hybrid electric vehicles (PHEVs) has prompted considerable development of high-performance rechargeable LIBs worldwide.^[2] As a consequence, electrode materials with a superior performance have become critical for creating high-performance LIBs, particularly in terms of reducing cost while maintaining or improving functionality. Under equilibrium conditions, the total capacity of LIBs can be expressed as^[4,5]

$$\text{Total Capacity} = \frac{1}{\frac{1}{C_A} + \frac{1}{C_C} + \frac{1}{Q_M}} \quad (1)$$

where C_A and C_C are the specific capacities of the cathode and anode materials, respectively, and $1/Q_M$ is the specific mass of the other cell components (electrolyte, separator, current collectors, case, etc.) with units of g mA h⁻¹.^[4,5] Currently, widely

investigated cathode materials, such as LiCoO₂, LiNiO₂, LiMn₂O₄, LiFe(Mn)PO₄ and LiCo_{1/3}Ni_{1/3}Mn_{1/3}O₂, are very limited in terms of their specific capacities (<300 mA h g⁻¹).^[6–8] Similarly, graphite, as a commercialized anode, is also hindering the development of LIBs, due to its low specific capacity of 372 mA h g⁻¹.^[9] Provided that the specific capacities of anode materials are increased up to 600 mA h g⁻¹, the total battery capacity can be distinctly enhanced.^[4,5] Therefore, there is an increasing interest in developing anode materials of high reversible capacity^[10] (such as Si,^[11,12] Sn^[13,14] and SnO₂^[15–17]) to replace graphite in LIBs.

It was recently reported that the SnO₂ anode can store over twice as much lithium as conventional graphite, accounting for one of the most promising candidates with a theoretical specific capacity of about 781 mA h g⁻¹.^[18,19] It is well documented that the electrochemical interaction between lithium and SnO₂ can be described in two steps:^[20,21]



In Equation 2, the SnO_2 anode electrochemically reacts with Li^+ , resulting in the formation of Sn and lithium oxide. In particular, the produced Li_2O can serve as a “cushion” to buffer the large volume change during alloying and dealloying with lithium,^[22] which is an important reason for the better cyclability of SnO_2 as compared to Sn. Kim et al.^[23] investigated the reaction sequence for the lithiation of both SnO and SnO_2 , including the formation of lithia in both cases. In Equation 3, conversely, Li^+ can insert into Sn to form Li_xSn ($x \leq 4.4$) alloys. The large atomic uptake, a 440% increase in the number of atoms in going from Sn to $\text{Li}_{4.4}\text{Sn}$, induces huge volume expansions (up to 259%).^[24,25] During charge/discharge processes, the repeated large expansion and contraction of the Sn lattice leads to cracking, crumbling and pulverization of the Sn particles, as well as a loss of electrical contact between active Sn and conductive additives or the electrode current collector or both.^[26,27] Researchers have tried using various metallic Sn^[28,29] and Sn-graphite composites^[30,31] to stabilize the system, and Sn deposited on Cu^[32] and polyacrylonitrile^[33] nanowires has yielded promising results. Ning et al.^[34] reviewed the use of mechanical-chemical methods (e.g., micromilling) to fabricate alloys and composites (including graphite) of Sn or SnO_2 for negative electrodes. To stabilize SnO_2 electrodes, various approaches have been attempted, including using nanosized SnO_2 ,^[35–38] SnO_2 -matrix composites^[39,40] and special nanostructured SnO_2 such as nanotubes^[41,42] and nanowires.^[43–45]

There have been a number of investigations associated with composite electrode materials comprising SnO_2 and graphite or disordered carbons. Lee et al.^[46] investigated the dispersion of both Sn and SnO on synthetic graphite electrodes. Chen et al.^[47] employed a sol-gel process to form a graphite core surrounded by a SnO_2 shell. Wang et al.^[48] described a method of forming a porous carbon/ SnO_2 nanocomposite monolithic structure and examined the cycle life at various discharge rates. A molten-salt preparation procedure was employed by Liu et al.^[49] to form carbon- SnO_2 composite electrodes. Li et al.^[50] described a procedure by which electrodes with a near 50:50 weight ratio of carbon: SnO_2 were formed using a phenolic resin and $\text{SnCl}_4 \cdot 5\text{H}_2\text{O}$ precursors, which showed promising results (518 mA h g^{-1} after 500 cycles).

As a new class of 2D carbon allotropes arranged in a hexagonal lattice with very strong sp^2 -hybridized bonds, graphene nanosheet (GNS) shows a very high surface area (2630 $\text{m}^2 \text{g}^{-1}$) and a high electrical conductivity (resistivity = $10^{-6} \Omega \text{cm}$).^[51,52] Recently GNS has attracted interest as a matrix to create SnO_2 -graphene hybrids to improve the cycle stability of LIBs.^[53–61] Thus a large amount of effort has been devoted to developing SnO_2 -graphene nanocomposites using various methods including solution-based synthesis,^[53–60] solvothermal methods,^[61] self-assembly^[62] and ultrasonic spray pyrolysis.^[63] For all of these techniques, it is difficult to control the uniform distribution of deposited SnO_2 on the GNS. In particular, controlling the ratio and morphology of the SnO_2 crystalline and amorphous phases is difficult. While of similar composition, amorphous SnO_2 differs significantly from crystalline SnO_2 .

The amorphous SnO_2 , because of its intrinsic isotropic nature relative to crystalline SnO_2 , can reduce the degradation of SnO_2 electrodes associated with the volume changes during charge/discharge processes. For the referenced synthesis techniques used to date, one cannot easily control the degree of crystallinity, and it is thus difficult to investigate the influence of SnO_2 crystallinity on lithium storage performance for LIBs. The atomic layer deposition (ALD) technique is a surface-controlled and layer-by-layer process, relying on two sequential self-terminating half-reactions.^[64] ALD shows significant promise for our purposes, as this method affords superior control over SnO_2 deposition with high flexibility and precision; specifically, ALD offers unrivaled precision in terms of controlling the ratio and morphology of the crystalline and amorphous phases of deposited SnO_2 .^[65] In this study, ALD was employed to deposit SnO_2 on GNS, and sandwich-like nanostructured composites of SnO_2 -GNS- SnO_2 were obtained and characterized. We also compared graphene composites with amorphous and crystalline SnO_2 as anodes in LIBs.

2. Results and Discussion

Composite anodes consisting of GNS and SnO_2 nanoparticles were cast on copper foils with a poly(vinylidene fluoride) (PVDF) binder, and the as-prepared negative electrodes were examined using X-ray diffraction (XRD). The degrees of crystallinity of the SnO_2 nanoparticles deposited on the GNS by means of ALD were determined from the XRD patterns: patterns a and c in Figure 1 are for ALD- SnO_2 at 400 °C and 200 °C, respectively. In pattern a in Figure 1, with the exception of the reflection peaks due to the copper current collector (50.7° and 59.3°), diffraction peaks are observed at $2\theta = 30.9^\circ$, 39.5°, 44.3°, 60.9° and 64.5°: these can be assigned to the SnO_2

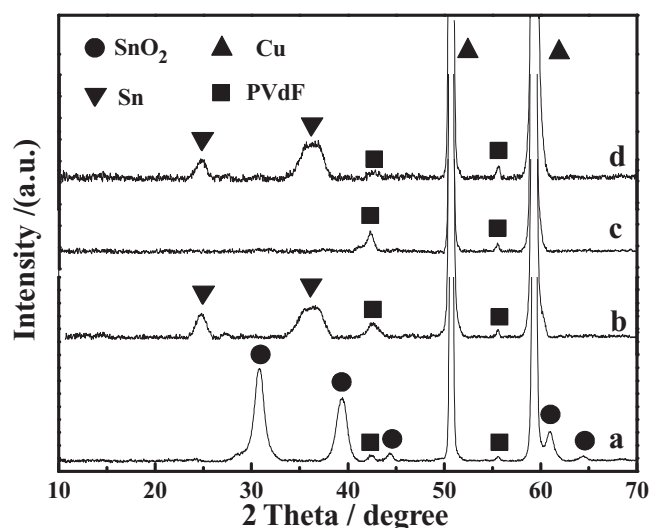


Figure 1. XRD patterns of (a,b) crystalline SnO_2 -GNS and (c,d) amorphous SnO_2 -GNS anodes (a,c) before and (b,d) after 150 charge/discharge cycles.

(110), (101), (200), (101), (211) and (220) faces, respectively (Joint Committee on Powder-Diffraction Standards (JCPDS) PDF No. 88-0827), which is representative of SnO_2 in the crystalline phase. The sharp diffraction peaks with high intensity indicate well-formed, crystalline SnO_2 . The XRD pattern based on powder (Figure S1a, Supporting Information) also confirms the formation of crystalline SnO_2 . In contrast, there is no concomitance of any diffraction line assigned to crystalline SnO_2 in pattern c in Figure 1. For the XRD pattern of SnO_2 -graphene via ALD at 200 °C (Figure S1b, Supporting Information), there is a considerably broadened peak between 20 to 45°, implying the amorphous nature of the deposited SnO_2 . Obviously, the growth temperature plays an important role in determining the degree of crystallinity of ALD- SnO_2 . The mechanisms have been elucidated in an earlier work.^[65] In addition, changes in the phase characteristics of the two anode materials are shown in patterns b and d in Figure 1 after charge and discharge cycles, respectively, which will be discussed later.

The as-prepared GNS presents an ultrathin, wrinkled and curved transparent gossamer-like structure consisting of around 10 layers of graphene (Figure S2, Supporting Information). The morphologies of the SnO_2 -GNS composite anodes were characterized by field-emission scanning electron microscopy (FE-SEM), transmission electron microscopy (TEM), and high-resolution TEM (HR-TEM), as shown in Figure 2. It is illustrated in Figure 2a,b that crystalline and amorphous SnO_2 were each homogeneously deposited on both sides of the GNS. Both composites possessed a layer-by-layer assembled structure of the SnO_2 particles, leading to sandwich-structured SnO_2 -GNS- SnO_2 composites. However, different growing temperatures led to different particle sizes of the deposited SnO_2 . It is seen that the dimensions of the crystalline SnO_2 nanoparticles were in the range of 30 to 40 nm, while the amorphous ones were in the range of 3 to 5 nm. The TEM images of Figure 2c,d further reveal that the SnO_2 nanoparticles were closely anchored on the surfaces of the GNS, even after the strong ultrasonic treatment for preparation of the TEM samples had been applied. Thus, a strong interaction between the SnO_2 nanoparticles and the GNS is indicated. Furthermore, the HR-TEM image of the crystalline SnO_2 in Figure 2e shows a basal space of 0.33 nm, which matches well with the (110) lattice fringes of crystalline SnO_2 (JCPDS PDF No. 44-0141). The inset of Figure 2e displays the corresponding selected-area electron diffraction (SAED) pattern of crystalline SnO_2 . The spotted diffraction rings from inside to outside could be indexed to the (110), (101), (200), and (211) planes of rutile SnO_2 , respectively, confirming the formation of crystalline SnO_2 deposited at 400 °C by ALD. In sharp contrast, there is no lattice fringing observed

in the HR-TEM image of Figure 2f, indicating the substantially amorphous state of the SnO_2 nanoparticles. The SAED pattern in the inset of Figure 2f shows a diffuse halo ring, thereby confirming the amorphous SnO_2 nanostructure formed at lower temperature (200 °C) in this work.

It is demonstrated in Equation 2 that SnO_2 can electrochemically decompose into Sn and Li_2O in the first discharge process. The XRD patterns b and d in Figure 1 confirm the structural changes of the crystalline and amorphous SnO_2 -GNS anodes, respectively, after 150 charge/discharge cycles at a current density of 400 mA g^{-1} between 0.01 and 3.00 V. For the crystalline SnO_2 -GNS, electrochemical cycling induced clear diffraction peaks located at about 25.0° and 35.8° in pattern b in Figure 1, belonging to the tetragonal Sn phase (JCPDS PDF No. 65-5224). In particular, there were no observable SnO_2 diffraction peaks, implying that the crystalline SnO_2 -GNS anode accomplished a full electrochemical transformation from SnO_2 to Sn. In pattern d in Figure 1, there are also two peaks corresponding to tetragonal Sn, which demonstrates that the crystalline Sn was formed in the electrochemical transformation of the amorphous SnO_2 with lithium. Furthermore, this electrochemical reaction

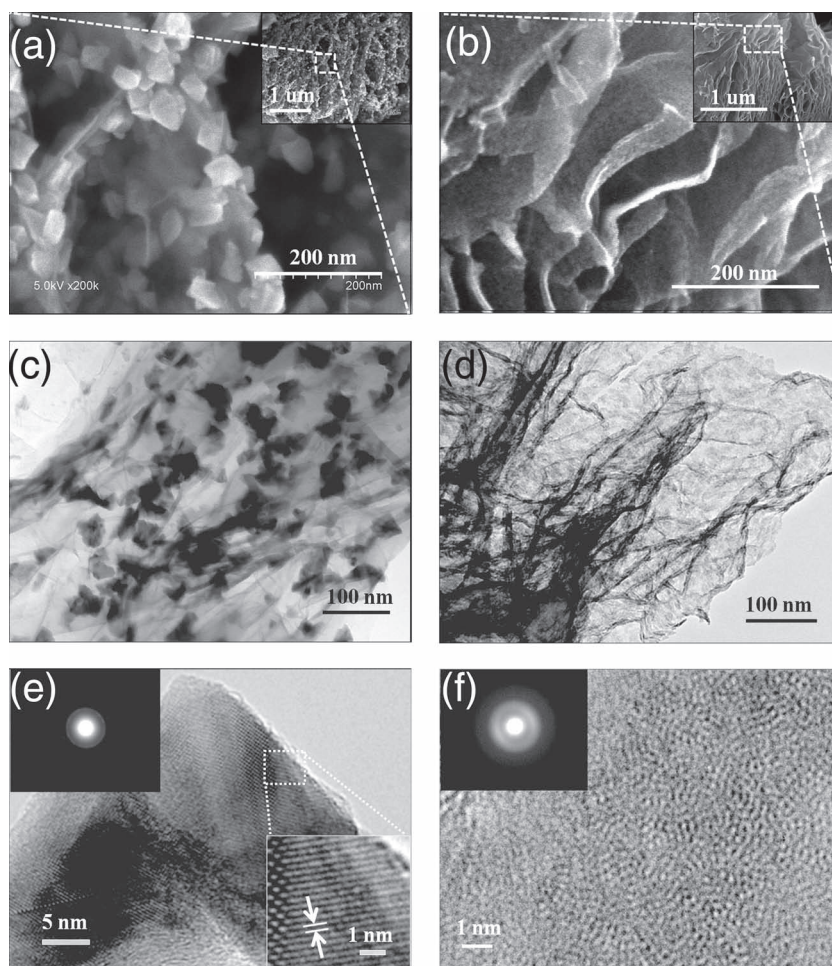


Figure 2. a,b) SEM observation of crystalline (a) and amorphous (b) SnO_2 -GNS. c,d) TEM observation of crystalline (c) and amorphous (d) SnO_2 -GNS. e,f) HR-TEM and SAED (inset) of crystalline (e) and amorphous (f) SnO_2 -GNS.

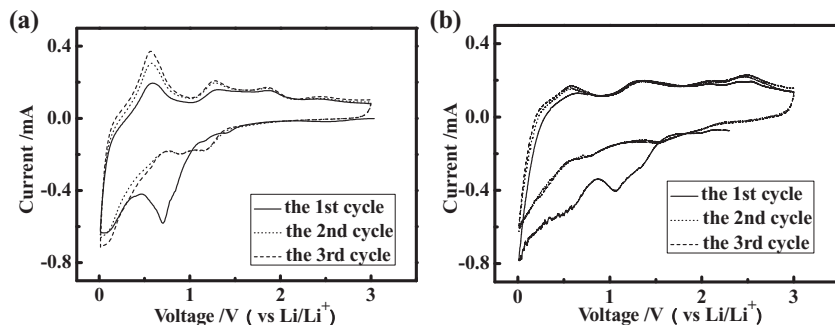


Figure 3. a,b) Cyclic voltammograms of the crystalline (a) and amorphous (b) SnO_2 -GNS anodes.

was confirmed by FTIR spectroscopy (Figure S3, Supporting Information). It has been reported that the absorption bands are located in the spectral region range of $500\text{--}700\text{ cm}^{-1}$ for the Sn–O–Sn vibration.^[66,67] Before electrochemical cycling, both the crystalline and amorphous SnO_2 showed a Sn–O–Sn vibration (Figure S3a and S3b, Supporting Information). The disappearance of these vibration bands indicates that the amorphous SnO_2 decomposed electrochemically into Sn after cycling. In the HR-TEM images of the crystalline and amorphous SnO_2 -GNS after 150 charge/discharge cycles (Figure S4, Supporting Information), the interplanar spacing of 0.29 nm corresponds to the distance of the neighboring (200) planes in tetragonal Sn.

The electrochemical properties of the crystalline and amorphous SnO_2 -GNS anodes were examined by cyclic voltammetry, yielding cyclic voltammograms (CVs) (see Figure 3a,b, respectively). A sweep rate of 0.1 mV s^{-1} was employed, with the voltage ranging from 0.01 to 3.00 V , in order to test the full range of the lithium storage behavior of SnO_2 -GNS. For the two anodes, their CV profiles of the 2nd and 3rd cycle are similar, but there was an obvious difference between the first cycle and longer-term cycling. In the first cycle, Equation 2 is not a reversible reaction due to the formation of Li_2O , leading to irreversible loss in capacity.^[68,69] The reaction between the anodes and the electrolyte results in solid-electrolyte-interphase (SEI) films over the surface of the anodes.^[70,71] These two factors yielded the current peak positioned at 0.75 V for the crystalline SnO_2 -graphene in the first cathodic scan and the one centered at about 1.05 V for the amorphous SnO_2 -graphene, but these peaks disappeared in subsequent cycles. Current peaks near 0 V might reflect Li–Sn alloying and lithium intercalation into the graphene layers.^[72]

Figure 4a,b show the voltage profiles generated by the crystalline and amorphous SnO_2 -GNS composite anodes in the 1st, 2nd, 50th, 100th and 150th cycles at a current density of 400 mA g^{-1} within a voltage window of $0.01\text{--}3.00\text{ V}$. The discharge (Li^+ insertion)

and charge (Li^+ extraction) of the crystalline SnO_2 -GNS composite occurred at 1686 and 968 mA h g^{-1} in the first cycle, respectively. The coulombic efficiency was 57.4% . In the second discharge process, the crystalline SnO_2 -GNS electrode exhibited a reversible capacity of 1042 mA h g^{-1} . The irreversible capacity loss of 38.2% in the first cycle might be due to two factors: the irreversibility of Equation 2 and the SEI-film formation. In comparison, the amorphous SnO_2 -GNS composite delivered a discharge capacity of 1366 mA h g^{-1} and a charge capacity of 677 mA h g^{-1} in the first cycle. Its initial coulombic efficiency and irreversible capacity

loss were 49.5% and 44.1% , respectively. Obviously, as illustrated by Figure 4a,b, the two electrodes show different lithium storage behaviors. The potential of the crystalline SnO_2 -GNS first dropped rapidly and then reached a plateau at 0.80 V during the first discharge, related to Equation 2 and the formation of the SEI film. After that, it continuously decreased down to 0.01 V , corresponding to Li–Sn alloying and Li^+ intercalation into the GNS, which is in good agreement with previous studies.^[73,74] However, the amorphous SnO_2 -GNS showed a sloping voltage region over the range of $1.38\text{--}0.81\text{ V}$, corresponding to the peak at about 1.05 V in Figure 3b, followed by a further voltage decrease to 0.01 V , similar to the crystalline SnO_2 -GNS.

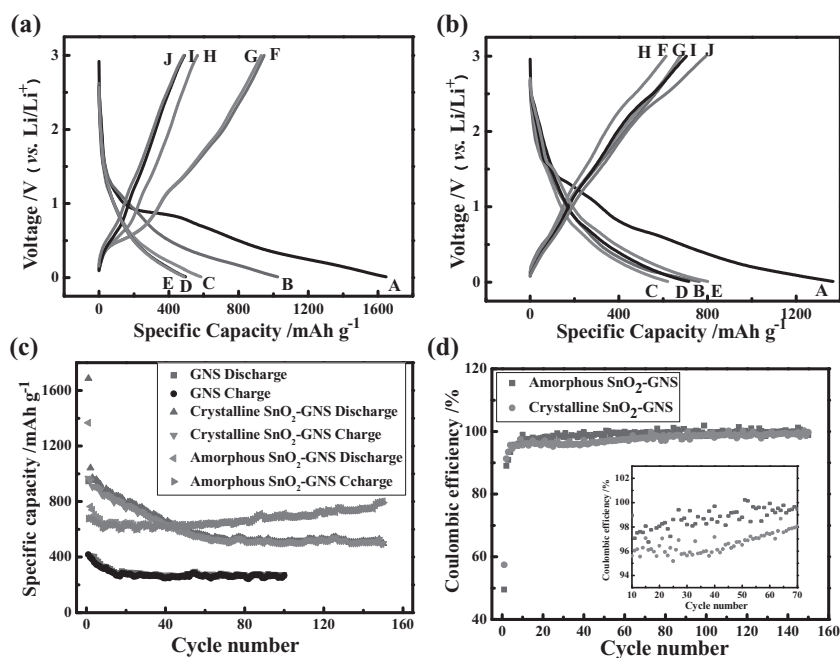


Figure 4. a,b) Charge/discharge profiles of crystalline (a) and amorphous (b) SnO_2 -GNS at a current density of 400 mA g^{-1} in a voltage window of $0.01\text{--}3.00\text{ V}$: the discharge curves in the 1st (A), 2nd (B), 50th (C), 100th (D), and 150th (E) cycles, and the charge curves in the 1st (F), 2nd (G), 50th (H), 100th (I), 150th cycles (J). c) Reversible charge/discharge capacities against cycle number for GNS at a current density of 100 mA g^{-1} in the voltage window of $0.01\text{--}3.00\text{ V}$, and for crystalline and amorphous SnO_2 -GNS at a current density of 400 mA g^{-1} in the voltage window of $0.01\text{--}3.00\text{ V}$. d) Coulombic efficiency against cycle number for crystalline and amorphous SnO_2 -GNS.

The cycle performance of the crystalline and amorphous SnO₂-GNS with a graphene matrix is compared in Figure 4c. The pure GNS shows not only the ordinary cycle performance, but also a lower specific capacity (269 mA h g⁻¹ in the 100th cycle). In comparison, the capacities of the amorphous and crystalline SnO₂-GNS composite anodes on cycling demonstrate different behaviors. For the crystalline SnO₂-graphene anode, the reversible capacity continuously decayed from the 1st to the 70th cycle. It is noteworthy that the discharge capacity tended to level off after 70 cycles and it could still deliver a reversible Li⁺ storage capacity of 499 mA h g⁻¹ after 150 cycles, a decrease of 52.2% in comparison to the value for the second cycle. For the amorphous SnO₂-graphene anode, however, the reversible capacity only decreased in the first 10 cycles, and then presented a slight but continuous increase with charge/discharge cycle. The reversible capacity of the amorphous SnO₂-GNS increased up to 793 mA h g⁻¹ by the 150th cycle, accounting for an increase by 4.8% in comparison to the second cycle, and a value about 115% higher than the theoretical capacity of graphite (372 mA h g⁻¹). Several tests have confirmed this trend. Extended cycling behavior for the amorphous SnO₂-GNS is shown in Figure S5, Supporting Information. Obviously, the amorphous SnO₂-GNS exhibited excellent cycle performance. Surprisingly, the specific capacity increased, reaching a maximum (821 mA h g⁻¹) at around the 194th cycle. In order to confirm the important influence of the amorphous phase on the electrochemical performance, the amorphous SnO₂-GNS nanocomposites were annealed, resulting in crystalline SnO₂-GNS. These two nanocomposites had the same SnO₂ loading on GNS and a similar SnO₂ particle size (Figure S6, Supporting Information). From our results, they showed different cycling performances (Figure S7, Supporting Information). As a consequence, different crystallinities (amorphous and crystalline) can result in different cyclabilities. Using the amorphous SnO₂ anode can effectively improve the cycling performance.

Furthermore, both anodes showed a different coulombic efficiency. The coulombic efficiency of the crystalline SnO₂-GNS changed from 95.6% in the 11th cycle to 98.1% in the 70th cycle and was close to 99% above 70 cycles (see Figure 4d). On the other hand, the amorphous SnO₂-GNS anode showed an improved coulombic efficiency increasing from 97% in the 11th cycle to 99.2% in the 50th cycle, and in particular, was close to effectively 100% in subsequent cycles. In comparison to the crystalline SnO₂-GNS, the amorphous SnO₂-GNS anode showed a higher coulombic efficiency upon cycling. In the first 70 cycles, the low coulombic efficiency of the crystalline SnO₂-GNS was due to its large volume change, resulting in the formed fresh surface area of the anodes during the charge/discharge process, increasing side reactions between the anodes and the electrolyte. Thus, the amorphous SnO₂-GNS composite shows a superior cycle stability as well as higher coulombic efficiency upon cycling.

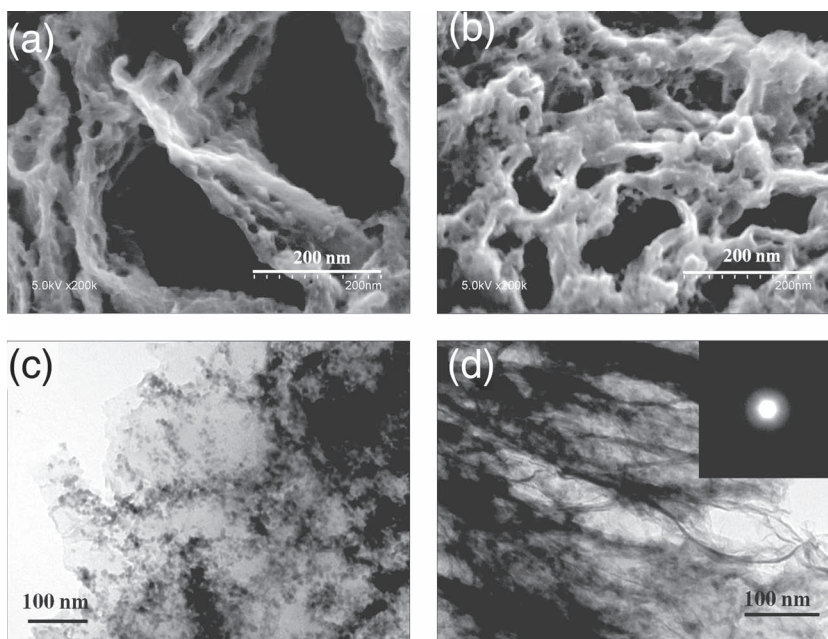


Figure 5. a,b) SEM images of crystalline (a) and amorphous (b) SnO₂-GNS after 150 cycles. c,d) TEM images of crystalline (c) and amorphous (d) SnO₂-GNS after 150 cycles. The inset in (d) is an SAED pattern confirming the crystalline nature of the resultant Sn material.

To confirm the evolution of the crystalline SnO₂-GNS and the amorphous SnO₂-GNS under robust mechanical force during the charge/discharge processes, we investigated changes in the morphology and structure of the cycled electrodes (delithiated at the end of cycling), using FE-SEM and TEM. Figure 5a and 5c show the SEM and TEM images of the crystalline SnO₂-GNS after 150 cycles using a 10 mV cut-off. Sn nanoparticles of 4 to 7 nm are observed in Figure 5c, where SnO₂ particles with a size of 30 to 40 nm were pulverized into smaller Sn nanoparticles due to the strong Sn-lattice expansion and contraction upon cycling, even though the GNS matrix was employed. The pulverization of the crystalline SnO₂ causes electric-contact loss between some of the Sn particles and the current collector, leading to the fading capacity in the first 70 cycles. Once the size of obtained Sn nanoparticles decreased to 4–7 nm due to the electrochemical pulverization, the smaller Sn particles effectively lowered the absolute volume change, improving the charge/discharge cyclability,^[75–77] and there was no obvious capacity loss from the 70th cycle to the 150th cycle, as shown in Figure 4c. The SAED pattern of amorphous SnO₂-GNS after 150 cycles, as shown in the inset in Figure 5d, indicates that the resultant Sn is substantially crystalline, which is in agreement with the XRD results of patterns c and d in Figure 1.

In the reaction of the amorphous SnO₂ with lithium, in contrast, the amorphous SnO₂ was less dense than its crystalline counterpart, and maintained an isotropic nature. Thus, the amorphous SnO₂ is associated with a homogeneous volume expansion and contraction, by eliminating the existence of two phase regions.^[78,79] As a result, the amorphous SnO₂ is better able to absorb the volume changes^[80] and shows less structural or mechanical strain and less pulverization caused by lattice volume changes than the crystalline one.^[81,82] Moreover,

for amorphous SnO₂, the initial particles have a smaller size range and, thereby, probably contribute to smaller absolute volume changes because the bigger SnO₂ particles exhibit a higher tendency to collapse and pulverization while cycling. In contrast, the GNS provides a matrix that effectively suppresses the smaller volume change of the amorphous SnO₂ anode.^[59,83] Furthermore, as is indicated in the thermogravimetric analysis (TGA) (Figure S8, Supporting Information), different ALD deposition temperatures result in different amounts of SnO₂ on the GNS. The amounts of SnO₂ deposited on the GNS may cause different cycling performances. In the case of a low loading of amorphous SnO₂ on the GNS, the high GNS amount in the nanocomposites as matrix can function as the cushion to buffer the volume change upon cycling more effectively, resulting in a better performance. Therefore, as shown in Figure 5b,d, after 150 cycles, the amorphous SnO₂-GNS electrode was apparently intact because of the effective suppression of the volume expansion and contraction, which is consistent with the amorphous SnO₂-GNS electrode exhibiting a better cycling performance.

To help understand the different behaviors of the lithium-storage processes, the morphological evolution of the crystalline SnO₂-GNS and the amorphous SnO₂-GNS is suggested in Scheme 1. GNS as a matrix can buffer SnO₂ volume changes in charge/discharge cycles to some extent, and, thereby, the crystalline SnO₂-GNS shows some improvement in cycling performance. However, the large volume expansion and shrinkage (as schematically illustrated in a2 and a3 in Scheme 1) causes some anode materials to lose their electrical contact with the GNS (as illustrated in a4 in Scheme 1). From this point of view, GNS as the matrix has some limitations and does not mitigate the detrimental effects due to the SnO₂ volume changes completely, accounting for the fading capacity in the first 70 cycles in Figure 4c. With regard to the amorphous SnO₂-GNS, the

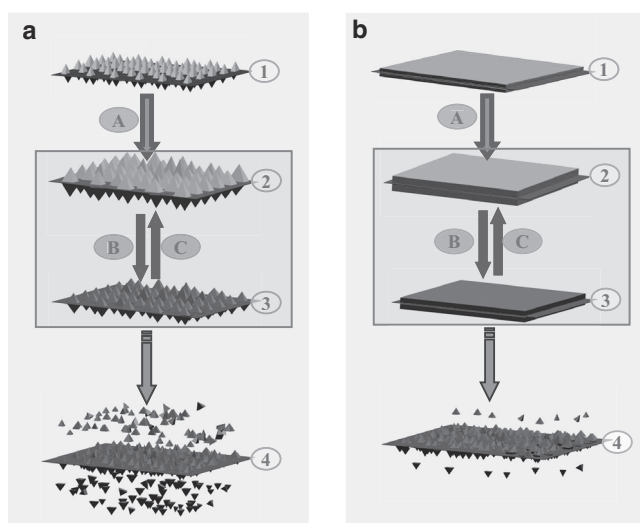
pristine SnO₂ is present in films deposited on both sides of the GNS (Scheme 1, b1). Upon electrochemical reaction with lithium, the amorphous SnO₂ films are broken up into small anode materials. In comparison with the crystalline SnO₂-GNS, the amorphous SnO₂ is intrinsically isotropic and less dense. As a consequence, with the help of GNS as the matrix, the amorphous SnO₂-GNS accommodates substantial volume changes and only a small fraction of anode material is lost due to electrical isolation from the GNS matrix (Scheme 1, b4). More importantly, morphological changes from films to nanoparticles can increase the contact area between the anodes and the electrolyte greatly, leading to a slightly increasing capacity with cycle number, as shown in Figure 4c.

3. Conclusions

This study demonstrates that ALD is capable of controlling the deposition of SnO₂ on GNS with different structural phases, resulting in amorphous and crystalline SnO₂-GNS composites with sandwich nanostructures. These two types of SnO₂-GNS composites were made into the anodes of LIBs, and both types exhibited a promising electrochemical performance. The crystalline SnO₂-GNS nanocomposite showed a discharge capacity of 499 mA h g⁻¹ after 150 cycles, although it was decreased by 52.2% in comparison with the second cycle. SEM and TEM results confirmed that this fading capacity of the crystalline SnO₂-GNS was mainly due to the pulverization of the SnO₂ crystals, while the amorphous SnO₂ could effectively buffer the huge volume expansion and shrinkage of the Sn lattice during the charge and discharge processes. Therefore, the amorphous SnO₂-GNS composites delivered a higher coulombic efficiency (close to effectively 100%), a high specific capacity (821 mA h g⁻¹ in the 194th cycle) and superior cycling stability. This work not only demonstrates that ALD is a useful approach for synthesizing anode materials of LIBs, but also shows that the structural phase of the anode material has an important influence on the electrochemical performance in LIB applications. Composites of graphene with amorphous SnO₂ show great promise as anode for LIBs.

4. Experimental Section

Synthesis of Graphene Nanosheets (GNS): Graphene oxide was prepared by the modified Hummers method^[84] as previously reported by our group.^[85,86] Graphite powder (1 g) was mixed with concentrated H₂SO₄ (23 mL), and stirred at room temperature for 0.5 h. NaNO₃ (0.5 g) was added, and the resulting mixture was left overnight. The reaction vessel was then immersed in an ice-water bath, and KMnO₄ (3 g) was added slowly, followed by stirring for 2 h. Subsequently, the mixture was stirred at 35 ± 3 °C for 3 h. After dilution with deionized (DI) water (46 mL), H₂O₂ (30%) was added to the mixture, and the color of the mixture changed to brilliant yellow, along with violent bubbling. Finally, the mixture was filtered and washed with an aqueous HCl solution to remove any residual metal ions, and was then further washed with DI water to reach a pH value of 7.0. The slurry was dried in air, yielding solid graphene oxide, which was placed in a quartz tube filled with flowing Ar gas, and exposed to a 30 s isothermal treatment by promptly moving the tube to an oven with a preheated temperature of 1050 °C. The tube was cooled to 50 °C in an Ar atmosphere. As a result, a material with fluffy and porous structures was produced, (i.e., graphene nanosheets (GNS)).



Scheme 1. Morphological evolution of (a) the crystalline SnO₂-GNS and (b) the amorphous SnO₂-GNS as the nanocomposite anodes in the charge/discharge cycles: the pristine SnO₂-GNS (1) transforms into GNS-based Li_xSn (2) after the first discharge (A); the alloying (2) and dealloying (3) of Li_xSn occur in the subsequent charge (B) and discharge (C) processes; with increased cycling number, some active materials lose electrical contact with GNS matrix, as illustrated in (4).

Synthesis of the Amorphous and Crystalline SnO₂-GNS Anodes: Amorphous and crystalline SnO₂-GNS composites were synthesized in an ALD reactor (Savannah 100, Cambridge Nanotechnology Inc., USA) under 0.4 Torr at 200 °C and 400 °C, respectively. More details have been previously reported by our group.^[65] Tin (IV) chloride (99% SnCl₄, Sigma–Aldrich) and DI water in two cylinders were used as the tin and oxygen sources, respectively. Nitrogen gas was used as the carrier gas with a flow rate of 20 sccm. A typical ALD cycle consisted of a sequential and alternating supply of SnCl₄ and water as follows: a 0.5 s supply of SnCl₄ vapor, a 3 s extended exposure of SnCl₄ to GNS, a 10 s N₂ purge, a 1 s supply of water vapor, a 3 s extended exposure of water vapor to GNS, another 10 s N₂ purge. To produce the aforementioned amorphous and crystalline SnO₂-GNS composites, the ALD processes were performed at low (200 °C) and high (400 °C) temperatures, respectively.

Structural Characterization: X-ray powder diffraction (XRD) patterns were collected on a Bruker D8 Discover Diffractometer using Co K_α radiation ($\lambda = 1.78897$ nm) at 40 kV and 100 mA. The morphologies and structures of the crystalline and amorphous SnO₂-GNS were observed using FE-SEM (Hitachi S-4800), TEM (Philips CM10) and HR-TEM (JEOL 2010 FEG). The Fourier transform infrared spectroscopy (FTIR) was performed by Bruker Tensor 27.

Electrode Preparation and Electrochemical Instrumentation: Working electrodes were prepared by slurry-casting on copper foils that served as current collectors. The slurry contained active material (crystalline SnO₂-GNS or amorphous SnO₂-GNS of 83.3 wt%, based on their dry solid mass) and a PVDF binder (16.7 wt% based on its dry solid mass) in *N*-methylpyrrolidinone (NMP) solvent. The electrodes were dried under vacuum at 90 °C overnight. The working electrodes were cut to 9/16 in. in diameter and the mass-loading density was 6.04 mg in.⁻². The electrolyte was composed of a 1 M LiPF₆ salt dissolved in ethylene carbonate (EC):diethyl carbonate (DEC):ethyl methyl carbonate (EMC) at a 1:1:1 volume ratio. Lithium foil was used as the counter electrode. CR-2325-type coin cells were assembled in a glove box (Vacuum Atmosphere Company) under a dry Ar atmosphere (moisture and oxygen concentration < 1 ppm). Cyclic voltammetry were performed on a CHI Electrochemistry workstation at a scan rate of 0.1 mV s⁻¹ over a potential range of 0.01 to 3.0 V (vs. Li/Li⁺). The charge/discharge characteristics were tested galvanostatically between 0.01 and 3.0 V (versus Li/Li⁺) at room temperature using an Arbin BT-2000 Battery Tester.

Supporting Information

Supporting Information is available from the Wiley Online Library or from the author.

Acknowledgements

This research was supported by the Natural Science and Engineering Research Council of Canada (NSERC), General Motors, the Canada Research Chair (CRC) Program, the Canadian Foundation for Innovation (CFI), the Ontario Research Fund (ORF), the Early Researcher Award (ERA) and the University of Western Ontario. X. L. is grateful to the Ontario PDF Program.

Received: May 12, 2011

Revised: October 31, 2011

Published online: February 3, 2012

- [1] P. G. Bruce, B. Scrosti, J. M. Tarascon, *Angew. Chem. Int. Ed.* **2008**, *47*, 2930–2946.
- [2] J. M. Tarascon, M. Armand, *Nature* **2001**, *414*, 359–367.
- [3] M. Yoshio, R. J. Brodd, A. Kozawa, *Lithium-Ion Batteries*, Springer, New York **2008**.
- [4] M. Yoshio, T. Tsumura, N. Dimov, *J. Power Sources* **2005**, *146*, 10–14.

- [5] U. Kasavajjula, C. S. Wang, A. J. Appleby, *J. Power Sources* **2007**, *163*, 1003–1009.
- [6] M. S. Whittingham, *Chem. Rev.* **2004**, *104*, 4271–4301.
- [7] A. S. Aricò, P. Bruce, B. Scrosati, J. M. Tarascon, W. Schalkwijk, *Nat. Mater.* **2005**, *4*, 366–377.
- [8] G. A. Nazri, G. Pistoria, *Lithium Batteries: Science and Technology*, Springer, New York **2009**.
- [9] J. R. Dahn, T. Zheng, Y. H. Liu, J. S. Xue, *Science* **1995**, *27*, 590–593.
- [10] R. A. Huggins, *Advanced Batteries: Materials Science Aspects*, Springer, New York **2009**.
- [11] C. K. Chan, H. L. Peng, G. Liu, K. Mcllwraith, X. F. Zhang, R. A. Huggins, Y. Cui, *Nat. Nanotechnol.* **2008**, *3*, 31–35.
- [12] M. Holzapfel, H. Buqa, W. Scheifele, P. Novák, F. M. Petrat, *Chem. Commun.* **2005**, 1566–1568.
- [13] G. Derrien, J. Hassoun, S. Panero, B. Scrosati, *Adv. Mater.* **2007**, *19*, 2336–2340.
- [14] W. M. Zhang, J. S. Hu, Y. G. Guo, S. F. Zheng, L. S. Zhong, W. G. Song, L. J. Wan, *Adv. Mater.* **2008**, *20*, 1160–1165.
- [15] Y. Idota, T. Kubota, A. Matsufuji, Y. Maekawa, T. Miyasaka, *Science* **1997**, *276*, 1395–1397.
- [16] X. W. Lou, Y. Wang, C. L. Yuan, J. Y. Lee, L. A. Archer, *Adv. Mater.* **2006**, *18*, 2325–2329.
- [17] A. Sivashanmugam, T. Premkumar, S. Gopukumar, N. G. Renganathan, M. Wohlfahrt-Mehrens, J. Garche, *J. Appl. Electrochem.* **2005**, *35*, 1045–1050.
- [18] S. M. Paek, E. J. Yoo, I. Honma, *Nano Lett.* **2009**, *9*, 72–75.
- [19] C. Wang, Y. Zhou, M. Y. Ge, X. B. Xu, Z. L. Zhang, J. Z. Jiang, *J. Am. Chem. Soc.* **2010**, *132*, 46–47.
- [20] X. W. Lou, C. M. Li, L. A. Archer, *Adv. Mater.* **2009**, *21*, 2536–2539.
- [21] P. Meduri, C. Pendyala, V. Kumar, G. U. Sumanasekera, M. K. Sunkara, *Nano Lett.* **2009**, *9*, 612–616.
- [22] E. Kim, D. Son, T. G. Kim, J. Cho, B. Park, K. S. Ryu, S. H. Chang, *Angew. Chem. Int. Ed.* **2004**, *43*, 5987–5990.
- [23] K. J. Kim, H. Lee, H. J. Sohn, *Electrochem. Commun.* **2009**, *11*, 2125–2128.
- [24] I. A. Courtney, J. R. Dahn, *J. Electrochem. Soc.* **1997**, *144*, 2045–2052.
- [25] S. H. Lee, M. Mathews, H. Toghiani, D. O. Wipf, C. U. Pittman, *Chem. Mater.* **2009**, *21*, 2306–2314.
- [26] M. Noh, Y. Kim, M. G. Kim, H. Lee, H. Kim, Y. Kwon, Y. Lee, J. Cho, *Chem. Mater.* **2005**, *17*, 3320–3324.
- [27] M. G. Kima, J. Cho, *J. Electrochem. Soc.* **2009**, *156*, A277–A282.
- [28] M. Wachtler, J. O. Besenhard, M. Winter, *J. Power Sources* **2001**, *94*, 189–193.
- [29] J. R. Dahn, R. E. Mar, A. Abouzeid, *J. Electrochem. Soc.* **2006**, *153*, A361–A365.
- [30] G. X. Wang, J. H. Ahn, M. J. Lindsay, L. Sun, D. H. Bradhurst, S. X. Dou, H. K. Liu, *J. Power Sources* **2001**, *97*, 211–215.
- [31] L. Balan, R. Schneider, P. Willmann, D. Billaud, *J. Power Sources* **2006**, *161*, 587–593.
- [32] X. Y. Zhao, Z. H. Xia, D. G. Xia, *Electrochim. Acta* **2010**, *55*, 6004–6009.
- [33] Y. Yu, Q. Yang, D. Teng, X. Yang, S. Ryu, *Electrochem. Commun.* **2010**, *12*, 1187–1190.
- [34] L. J. Ning, Y. P. Wu, S. B. Fang, E. Rahm, R. Holze, *J. Power Sources* **2004**, *133*, 229–242.
- [35] M. S. Park, Y. M. Kang, G. X. Wang, S. X. Dou, H. K. Liu, *Adv. Funct. Mater.* **2008**, *18*, 455–461.
- [36] Y. D. Wang, I. Djerdj, B. Smarsly, M. Antonietti, *Chem. Mater.* **2009**, *21*, 3202–3209.
- [37] J. K. Shon, H. Kim, S. S. Kong, S. H. Hwang, T. H. Han, J. M. Kim, C. Pak, S. Doo, H. Chang, *J. Mater. Chem.* **2009**, *19*, 6727–6732.
- [38] C. Zheng, X. Zheng, Z. Hong, X. Ding, M. Wei, *Mater. Lett.* **2011**, *65*, 1645–1647.

- [39] X. W. Lou, D. Deng, J. Y. Lee, L. A. Archer, *Chem. Mater.* **2008**, *20*, 6562–6566.
- [40] H. X. Zhang, C. Feng, Y. C. Zhai, K. L. Jiang, Q. Q. Li, S. S. Fan, *Adv. Mater.* **2009**, *21*, 2299–2304.
- [41] Y. Wang, H. C. Zeng, J. Y. Lee, *Adv. Mater.* **2006**, *18*, 645–649.
- [42] Y. Wang, J. Y. Lee, H. C. Zeng, *Chem. Mater.* **2005**, *17*, 3899–3903.
- [43] W. W. Zhou, C. W. Cheng, J. P. Liu, Y. Y. Tay, J. Jiang, X. T. Jia, J. X. Zhang, H. Gong, H. H. Hng, T. Yu, H. J. Fan, *Adv. Funct. Mater.* **2011**, 212439–2445.
- [44] H. Kim, J. Cho, *J. Mater. Chem.* **2008**, *18*, 771–775.
- [45] Y. D. Ko, J. G. Kang, J. G. Park, S. Lee, D. W. Kim, *Nanotechnology* **2009**, *20*, 455701.
- [46] J. Y. Lee, R. Zhang, Z. Liu, *J. Power Sources* **2000**, *90*, 70–75.
- [47] Y. C. Chen, J. M. Chen, Y. H. Huang, Y. R. Lee, H. C. Shih, *Surf. Coat. Technol.* **2007**, *202*, 1313–1318.
- [48] Z. Wang, M. A. Fierke, A. Stein, *J. Electrochem. Soc.* **2008**, *155*, A658–A663.
- [49] B. Liu, Z. P. Guo, G. Du, Y. Nuli, M. F. Hassan, D. Jia, *J. Power Sources* **2010**, *195*, 5382–5386.
- [50] M. Y. Li, C. L. Liu, Y. Wang, W. S. Dong, *J. Electrochem. Soc.* **2011**, *158*, A296–A301.
- [51] A. H. Castro Neto, F. Guinea, N. M. R. Peres, K. S. Novoselov, A. K. Geim, *Rev. Mod. Phys.* **2009**, *81*, 109–162.
- [52] D. Chen, L. Tang, J. Li, *Chem. Soc. Rev.* **2010**, *39*, 3157–3180.
- [53] X. Y. Wang, X. F. Zhou, K. Yao, J. G. Zhang, Z. P. Liu, *Carbon* **2011**, *49*, 133–139.
- [54] L. S. Zhang, L. Y. Jiang, H. J. Yan, W. D. Wang, W. Wang, W. G. Song, Y. G. Guo, L. J. Wan, *J. Mater. Chem.* **2010**, *20*, 5462–5467.
- [55] M. Zhang, D. N. Lei, Z. F. Du, X. M. Yin, L. B. Chen, Q. H. Li, Y. G. Wang, T. H. Wang, *J. Mater. Chem.* **2011**, *21*, 1673–1676.
- [56] H. Kim, S. W. Kim, Y. U. Park, H. Gwon, D. H. Seo, Y. Kim, K. Kang, *Nano Res.* **2010**, *3*, 813–821.
- [57] Z. Y. Wang, H. Zhang, N. Li, Z. J. Shi, Z. N. Gu, G. P. Cao, *Nano Res.* **2010**, *3*, 748–756.
- [58] Y. M. Li, X. J. Lv, J. Lu, J. H. Li, *J. Phys. Chem. C* **2010**, *114*, 21770–21774.
- [59] J. Yao, X. P. Shen, B. Wang, H. K. Liu, G. X. Wang, *Electrochem. Commun.* **2009**, *11*, 1849–1852.
- [60] Z. F. Du, X. M. Yin, M. Zhang, Q. Y. Hao, Y. G. Wang, T. H. Wang, *Mater. Lett.* **2010**, *64*, 2076–2079.
- [61] X. D. Huang, X. F. Zhou, L. Zhou, K. Qian, Y. H. Wang, Z. P. Liu, C. Z. Yu, *ChemPhysChem* **2011**, *12*, 278–281.
- [62] D. H. Wang, R. Kou, D. W. Choi, Z. G. Yang, Z. M. Nie, J. Li, L. V. Saraf, D. H. Hu, J. G. Zhang, G. L. Graff, J. Liu, M. A. Pope, I. A. Aksay, *ACS Nano* **2010**, *4*, 1587–1595.
- [63] T. Lu, Y. P. Zhang, H. B. Li, L. K. Pan, Y. L. Li, Z. Sun, *Electrochim. Acta* **2010**, *55*, 4170–4173.
- [64] S. M. George, *Chem. Rev.* **2010**, *110*, 111–131.
- [65] X. Meng, D. Geng, J. Liu, M. N. Banis, Y. Zhang, R. Li, X. Sun, *J. Phys. Chem. C* **2010**, *114*, 18330–18337.
- [66] F. M. Liu, B. F. Quan, L. H. Chen, L. X. Yu, Z. Q. Liu, *Mater. Chem. Phys.* **2004**, *87*, 297–300.
- [67] L. M. Fang, X. T. Zu, Z. J. Li, S. Zhu, C. M. Liu, W. L. Zhou, L. M. Wang, *J. Alloys Compd.* **2008**, *454*, 261–267.
- [68] T. Moon, C. Kim, S. T. Hwang, B. Park, *Electrochem. Solid-State Lett.* **2006**, *9*, A408–A411.
- [69] M. S. Park, G. X. Wang, Y. M. Kang, D. Wexler, S. X. Dou, H. K. Liu, *Angew. Chem. Int. Ed.* **2007**, *46*, 750–753.
- [70] X. W. Lou, J. S. Chen, P. Chen, L. A. Archer, *Chem. Mater.* **2009**, *21*, 2868–2874.
- [71] Z. H. Wen, Q. Wang, Q. Zhang, J. L. Li, *Adv. Funct. Mater.* **2007**, *17*, 2772–2778.
- [72] C. C. Chang, S. J. Liu, J. J. Wu, C. H. Yang, *J. Phys. Chem. C* **2007**, *111*, 16423–16427.
- [73] D. Deng, J. Y. Lee, *Chem. Mater.* **2008**, *20*, 1841–1846.
- [74] S. B. Yang, X. L. Feng, L. Wang, K. Tang, J. Maier, K. Mullen, *Angew. Chem. Int. Ed.* **2010**, *49*, 4795–4799.
- [75] I. A. Courtney, J. R. Dahn, *J. Electrochem. Soc.* **1997**, *144*, 2943–2948.
- [76] M. Winter, J. O. Besenhard, *Electrochim. Acta* **1999**, *45*, 31–50.
- [77] K. T. Lee, Y. S. Jung, S. M. Oh, *J. Am. Chem. Soc.* **2003**, *125*, 5652–5653.
- [78] J. P. Maranchi, A. F. Hepp, P. N. Kumta, *Electrochem. Solid-State Lett.* **2003**, *6*, A198–A201.
- [79] J. T. Yin, M. Wada, K. Yamamoto, Y. Kitano, S. Tanase, T. Sakai, *J. Electrochem. Soc.* **2006**, *153*, A472–A477.
- [80] Q. Fan, P. J. Chupas, M. S. Whittingham, *Electrochem. Solid-State Lett.* **2007**, *10*, A274–A278.
- [81] L. F. Cui, R. Ruffo, C. K. Chan, H. Peng, Y. Cui, *Nano Lett.* **2009**, *9*, 491–495.
- [82] S. W. Song, K. A. Striebel, X. Y. Song, E. J. Cairns, *J. Power Sources* **2003**, *119–121*, 110–112.
- [83] G. X. Wang, B. Wang, X. L. Wang, J. Park, S. X. Dou, H. Ahn, K. Kim, *J. Mater. Chem.* **2009**, *19*, 8378–8384.
- [84] W. S. Hummers, R. E. Offeman, *J. Am. Chem. Soc.* **1958**, *80*, 1339.
- [85] D. Geng, Y. Chen, Y. Chen, Y. Li, R. Li, X. Sun, S. Ye, S. Knights, *Energy Environ. Sci.* **2011**, *4*, 760–764.
- [86] X. Li, D. Geng, Y. Zhang, X. Meng, R. Li, X. Sun, *Electrochem. Commun.* **2011**, *13*, 822–825.